

An Automated Method for Inferring 3-D Salt Movements from the Suprasalt Sedimentation Pattern

Reinold R. Cornelius

GSCI Consulting, Austin, Texas, U.S.A.

Lawrence M. Cathles III

Cornell University, Ithaca, New York, U.S.A.

Alex Erendi

Cornell University, Ithaca, New York, U.S.A.

ABSTRACT

The formation and diapiric destruction of salt canopies have a direct impact on fluid flow and hydrocarbon migration in areas such as the Gulf of Mexico. Inferring the history and pattern of salt redistribution in even a local area can be time-consuming and is subject to uncertainties of many kinds. We demonstrate in this chapter that it is possible to infer the gross 3-D pattern of salt redistribution and the time when salt welds form directly from the sedimentation pattern and the present position of salt welds. The algorithm is based on the simple assumption that after isostatic adjustment is taken into account, accommodation space in areas with greater than average sediment loading is provided by salt movement to areas of less than average sediment loading. Although the algorithm is crude in several regards and could be improved by interpreter intervention, we show that the 2-D history of salt redistribution it estimates is almost identical to published salt migration histories inferred by conventional means in one test area. Applying the methods to a 20- × 50-km area in the offshore Louisiana Gulf of Mexico, we find that the 3-D simulation estimates salt-weld formation at significantly later time in the Eugene Island Block 330 area (0.45 versus 1.3 Ma) than 2-D simulations. The later time is more compatible with geochemical indications of late filling for the Eugene Island Block 330 reservoirs. The estimated timing of salt-weld formation does not depend on the present thickness of salt. Modeling subsalt pore-water movement through microdarcy subsalt strata indicates that brines can be drawn to early-opening salt from distances of 50 km or more.

INTRODUCTION

We have developed an automated method for reconstructing salt movements in the offshore

Louisiana Gulf of Mexico. This chapter presents the method and critically compares the basin histories it produced with the interpretations that others have obtained by completely different and

independent means. Our method is discussed in the context of recent salt tectonic concepts. Our purpose in estimating salt movements is to evaluate the effect of those movements on aqueous and hydrocarbon fluid flow. Consequently, this chapter includes an example of salt-directed fluid-flow simulation on a regional scale in the Gulf of Mexico.

Ever since Humphris (1978) recognized that the salt in the Gulf of Mexico did not rise into diapirs from a deeply buried autochthonous salt sheet but instead migrated both vertically and laterally to progressively shallower allochthonous salt masses, modeling concepts have been sought to describe this process (e.g., Jackson and Cornelius, 1987; Talbot, 1992). Genetic concepts of salt tectonics such as salt canopy formation (Jackson et al., 1987, 1990) have been applied successfully to the Gulf of Mexico (Talbot, 1993; Rowan, 1995; Rowan et al., 1994). Ultimately, the recognition of the importance of the interplay between sedimentation and salt movement led to a revolution in salt tectonics (Jackson, 1997), in which salt kinematics is described as a response to sediment loading (Vendeville and Jackson, 1992a, 1992b). Recent work has left little doubt that the development of petroleum systems is intimately linked to the formation and tectonics of allochthonous salt in the Gulf of Mexico (McBride et al., 1998; Cornelius et al., 1993a).

The work described in this chapter focused on devising an automatic salt redistribution scheme suited for finite-element fluid-flow modeling (Cornelius et al., 1993b). We follow Nelson's (1991) concept of passive salt rise driven by differential sediment loading. Our scheme coincides closely with Vendeville and Jackson's concept of passive diapirism. Deviations from the average sedimentation rate at each time step drive the redistribution of salt. The salt volume at the start of a simulation is the minimum which replicates the present-day salt position and thickness at the end of the simulation. The method estimates the history of salt movement, including the timing of salt-weld formation. Because the algorithm is driven entirely by the sediment record, it is fully automatic and requires no user input.

Our model relates to common salt dynamic terminology in the following fashion: "Salt rise" in our model results from what is called "down-building" in Gulf Coast salt literature (Jackson and Talbot, 1991). "Salt fall" occurs in our models where sedimentation rates are above average. "Salt

burial" in our models occurs where sedimentation rates are average. At this time, we do not model salt overhangs or pinched-off salt bodies, multilevel salt sheets, or multiple salt feeders. We do not model reactive or active diapirs (Vendeville and Jackson, 1992a); salt buoyancy is not accounted for in our model. We calculate redistribution of salt from a single salt layer. We do not honor the dynamic requirement of basin extension for Vendeville and Jackson's passive salt rise. One objective of this chapter is to evaluate the degree to which the salt-history reconstruction is affected by the lack of section extension, salt buoyancy, and other features not included in the algorithm.

The automated 3-D salt redistribution algorithm we describe is one in a set of tools compiled and developed by the Global Basins Research Network (GBRN) in a comprehensive modeling package called *BasinLAB*. The *BasinLAB* package consists of three broad components: A preprocessor infers the geologic evolution of the basin by backstripping, decompacting, calculating isostatic adjustments with specified lithospheric flexural rigidity, reconstructing fault movement, and inferring salt movements. A finite element solver computes fluid flow and hydrocarbon migration in the evolving grid specified by the preprocessor. Simulated 2-D and 3-D results are visualized with a DataExplorer visualization package. The finite element part of *BasinLAB* can function as a stand-alone solver (e.g., Roberts et al., 1996) or can be used with its preprocessor front end (Cipriani et al., 1993; Cornelius et al., 1994). The salt redistribution algorithm we describe and illustrate in this chapter is part of the preprocessor component of *BasinLAB*. We will first describe the salt redistribution algorithm and then illustrate its use by applying it to two areas of the offshore Louisiana Gulf of Mexico.

THE SALT MIGRATION ALGORITHM

Our salt redistribution algorithm assumes that salt moves in response to differential sediment loading. We decompact and backstrip the sediments in 1-D using a linear compaction-effective stress relation (see Appendix A), and we calculate isostatic adjustment in each 2-D section using methods described in Turcotte and Schubert (1982). We calculate the depression at the top of salt surface in each 2-D section at each time step that is required by the added sediment load and is not accommodated by isostasy. We assume that these

needs for residual accommodation space are met by salt movement. Consequently, we move salt from areas of higher than average to lower than average depression at the top of salt. We determine the minimum thickness of salt required by sediment deposition for each 2-D section, and then equalize this minimum redistribution between all 2-D lines in the 3-D volume by trading salt between lines. The result is that accommodation space for the observed pattern of sedimentation is provided by the smallest and most uniform redistribution of salt possible. At this point in the procedure, the salt volume is fully conserved. Finally, we add the constraint that salt welds, once formed, cannot reflate. This means that salt is lost from the section and that the salt volume is no longer conserved. Salt may be thought of as dissolved or “squeezed” oceanward in a geologically reasonable manner. The constraint of no reflation is imposed numerically. Once a new weld has formed, it cannot reflate.

Faulting is included in the salt redistribution algorithm in the following manner: As with the salt, strata offsets across faults are dictated by differences in the appropriately compacted sedimentation. Growth faultlike offsets are modeled in each 2-D section by maintaining constant fault width between the two parallel wells that define the fault. The right-hand side of a fault is displaced to the right so that a constant fault width is maintained from the left side of the fault. Section length is not preserved within the first element on the right side of a fault. In the strict structural sense, this strain should be resolved by a lateral translation of all nodes to the section edge on the right. For this reason, we use the term *growth faultlike*. No significant errors are introduced in the fluid-flow calculations, because our flow equations are referenced to stratigraphy, and flow is calculated at each time step on a static grid. Given all the uncertainties involved in salt reconstruction, we believe these deficiencies are outweighed by the ease provided by an automatic salt reconstruction algorithm, which can screen large areas quickly and can highlight subregions for alternate methods of analysis.

In this chapter, we first demonstrate the salt redistribution algorithm with a simple example. We then show that in at least one area of the Gulf of Mexico, our automatic algorithm estimates patterns of salt redistribution virtually identical to those obtained by others. We then apply the algorithm in estimating salt redistribution and fluid

flow on a regional scale in the offshore Louisiana Gulf of Mexico.

SIMPLE APPLICATION OF THE SALT REDISTRIBUTION ALGORITHM

Our salt redistribution algorithm is illustrated by a simple 3-D synthetic case in Figure 1. In this example, a fault cuts diagonally across the 3-D model domain so that the salt diapir broadens toward the front of the page and the salt withdrawal minibasin widens toward the back. The present-day geometry of the salt layer is shown in isometric perspective at the top of the figure, and the three east-west cross sections of which it is composed are shown below the isometric diagram. The stratigraphy consists of one sand layer (white) and two shale layers (gray). The system evolves by salt redistribution within a salt layer initially of uniform thickness.

The minimum salt thickness required to accommodate the sedimentation pattern for each 2-D section is shown at the bottom left. Where the minibasin is broad and the diapir narrow, the required salt thickness is thin. Where the diapir is broad and the minibasin thin, the required salt thickness is thick. When considered one 2-D section at a time, the original (reconstructed) salt layer would be thickest in the south (front of the page) and thinnest in the north.

The equalized minimum salt redistribution is shown at the right of the lower diagram. Here, we have traded salt from section to section, so that the total distribution is not only at a minimum but is equalized between sections. The accommodation space is now provided by a salt layer of initially uniform thickness.

THE AREAS MODELED

We now discuss two regional scale models. Both models contain South Eugene Island Block 330 (Figure 2). Block 330 is of specific interest for our modeling effort because of its giant oil field (Alexander and Flemings, 1995; Coelho, 1997) and because of the amount of research directed at this area by the GBRN and others. Both models are constructed from sets of approximately parallel 2-D sections.

The largest scale model, which we refer to as the “3-D regional model,” is 117 km in east-west

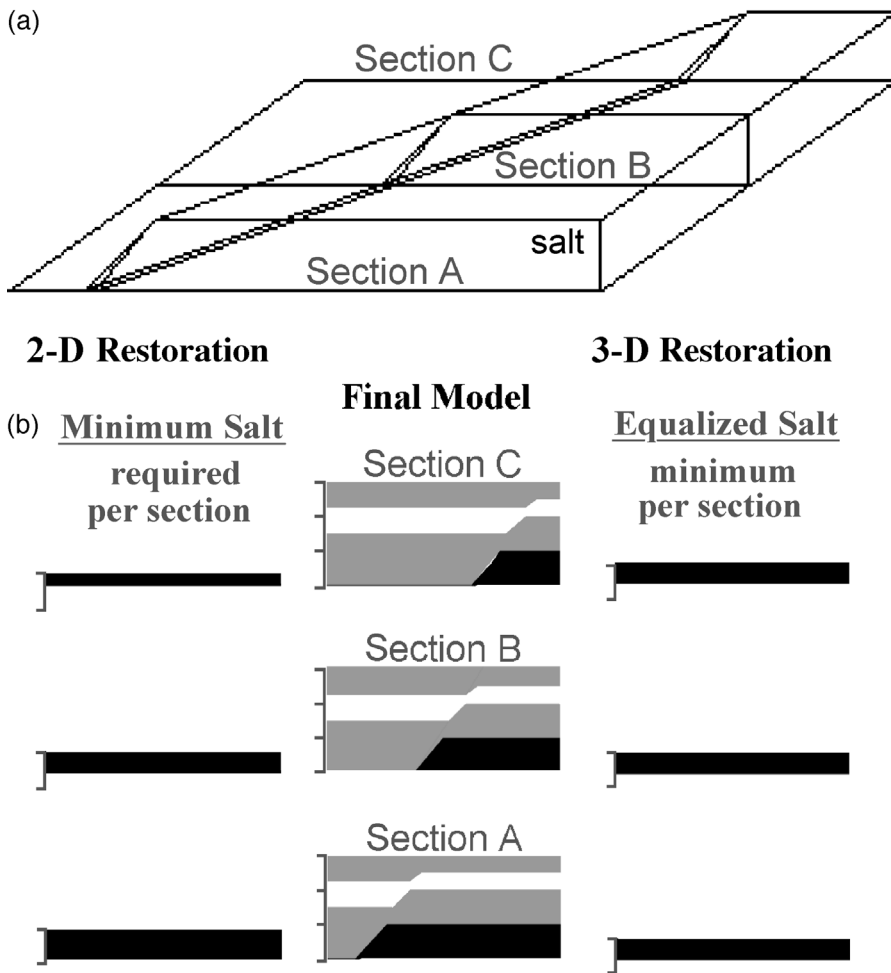


Figure 1. Salt redistribution is estimated by moving the minimum amount of salt required to provide accommodation space for sediments in each 2-D section and then equalizing the redistributed salt in three dimensions. (a) Perspective view of the final configuration of salt in a simple model. (b) Present configuration of all strata in the three east-west sections that comprise the upper figure. Salt is black, shale is gray, and sand is white. The minimum thickness of a uniform salt layer required to provide accommodation space for each 2-D section is shown to the left of the bottom sections. The equalized salt thicknesses are shown on the right. The volume of salt here is the same, but salt has been traded between sections so that the initial thickness of the salt layer is the same. The initial salt layer may be of variable thickness and welded in places, as discussed in the text.

dimension and extends from the Louisiana coast-line 223 km south to the base of the continental slope (Figure 2). The geology is captured by 26 subparallel 2-D north-south section lines (lines 33 and 35 are discussed and shown below). The sections are indicated in Figure 2 by dots at the locations of the 37 vertical “pseudowells” that define them. Stratigraphic horizons are captured in each well at 14 nodes. The uppermost 11 horizons have stratigraphic ages of 0.0, 0.45, 0.75, 1.3, 1.7, 2.8, 3.7, 4.0, 5.6, 8.3, and 13.4 Ma, respectively. The present-day bathymetry is defined by data describing the location of the shelf break throughout time, as well as the length of the continental slope and the slopes of continental shelf, slope, and abyssal plain. These data are assumed to be constant through time. The paleoposition of the shelf break shifts with time, as suggested by Galloway et al. (1991). Water depth variations are smooth. We ignore local topography on the seafloor in our modeling. It could be added easily, but in the cases presented, it was ignored.

The second 3-D “minibasin model,” shown by the gray lines in the smaller box in the Eugene Island South Addition area of Figure 2, is 18 km east-west by 50 km north-south. It contains 12 subparallel north-south sections, of which each has 34 vertical or nonvertical pseudowells. The 15 nodes in each pseudowell define 15 horizons. Three subsalt strata are truncated against the minibasin floor. The seven suprasalt strata are defined as time-stratigraphic horizons, with ages, from top to bottom, of 0.0, 0.4, 0.8, 1.1, 1.4, 1.9, 2.6, 3.0, and 3.8 Ma. Horizons defining the top and bottom of salt and the base of the section complete the 15 horizons. The geologic interpretation is taken from Rowan (1995). He characterizes this minibasin as “typical” of salt withdrawal minibasins on the outer shelf. The minibasin model does not include time and space variations in bathymetry. This does not affect the salt redistribution and weld formation, but shelf-break propagation as well as local seabed topography should be included in more complete models of this basin.

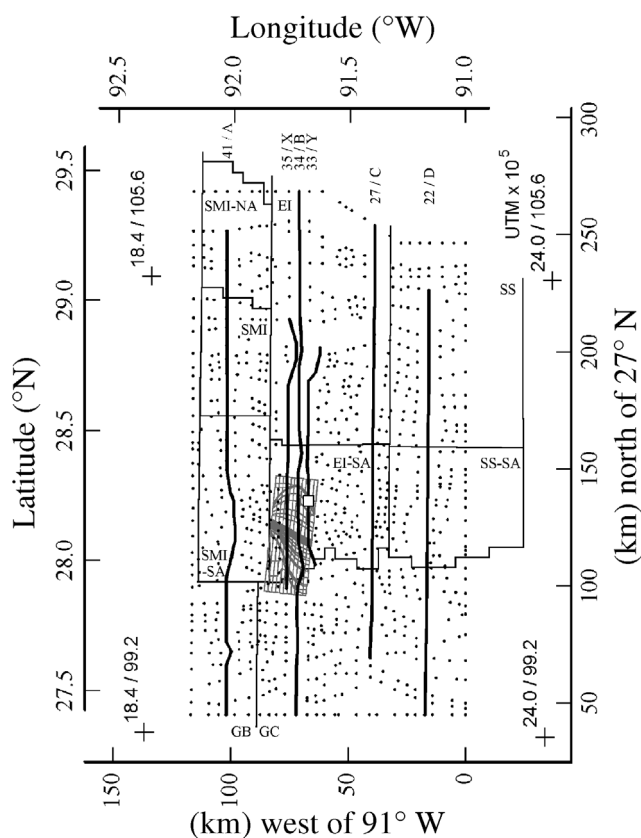


Figure 2. Location map for two regional models. Axes show longitudes and latitudes, as well as kilometers north of latitude 27°N and west of longitude 91°W. Four reference points to the Universal Transverse Mercator (UTM) system are given. Black dots show the location of the vertical pseudowells of the Gulf of Mexico 3-D regional model. The minibasin model grid is shown as a dense set of gray solid lines within a rectangular box. South Eugene Island 330 is shown as a white square contained by both models. Interpreted seismic lines used in the study are labeled with capital letters. Lines A, B, C, and D were contributed by ARCO to the GBRN. Lines X and Y are from Rowan (1996). Lease block divisions are indicated. EI = Eugene Island; SMI = South Marsh Island; SS = Ship Shoals; NA = North Addition; SA = South Addition; GB = Garden Banks; GC = Green Canyon.

TESTING THE AUTOMATIC SALT REDISTRIBUTION ALGORITHM

We test our salt migration algorithm by calculating the salt redistribution in Rowan's (1995) minibasin (small box in Figure 2). A geologic map of the minibasin is shown in Figure 3. The minibasin is defined by a regional, south-dipping fault in the north and a counterregional fault in the south,

which rests on top of a large salt mass. An antithetic fault within the minibasin dips north and joins the regional fault at depth. These listric faults are modeled by nonvertical wells. In three dimensions, the regional and counterregional faults are concave toward the basin. The antithetic fault is fairly straight. The basin, which has a bowl shape, is flooded by a salt-weld surface that is concave upward. There is a remnant, deep salt mass in the western part of the basin, underneath the antithetic fault. The basin is bordered in the east by a large salt mass (Figure 3).

The concave-upward character of the salt weld, e.g., the fact that the salt-weld dips into the basin from all sides, is explained by Rowan as resulting from salt evacuation from a bulb-shaped salt canopy. Minibasin formation and sediment fill are typically accompanied by throw on a regional fault bordering the basin on the proximal (northern) side and a secondary salt body, a "salt tongue," on the distal, downdip (southern) side. Observation of near-horizontal subweld sediments is crucial evidence that the basin evolved from a salt canopy. The subweld strata are typically truncated against the weld surface.

We calculate the salt redistribution in 3-D using the 12 sections through Rowan's geology, described above, and their traces, shown in Figure 2. The calculations are carried out as described and illustrated in the heuristic 3-D example above. The results of the modeling are shown in isometric block diagram form in Figure 4. Details of the faulting are presented in Figures 5 and 6. Our salt migration results are compared with Rowan's along one section taken from the 3-D reconstruction. It is section 8 in our model (Figure 3). Figures 7 and 8 compare our salt migration to Rowan's along this section.

Before comparing the models in detail, we would emphasize three points: (1) Our algorithm automatically infers the original salt-weld distribution, as well as its subsequent movements, from the present-day salt distribution and the pattern of sedimentation. (2) Rowan infers the original salt distribution and its movements by completely independent means, using the GEOSEC modeling tool (Rowan, 1993). (3) Rowan's model is 2-D, whereas ours is 3-D.

The results of our modeling are shown in isometric perspective in Figure 4. The salt thickness is shown at three periods by vertical bars attached to the base of salt. The lack of shading of the salt base indicates where salt welds have formed. A bulbous salt canopy lies at the surface (step 0 in

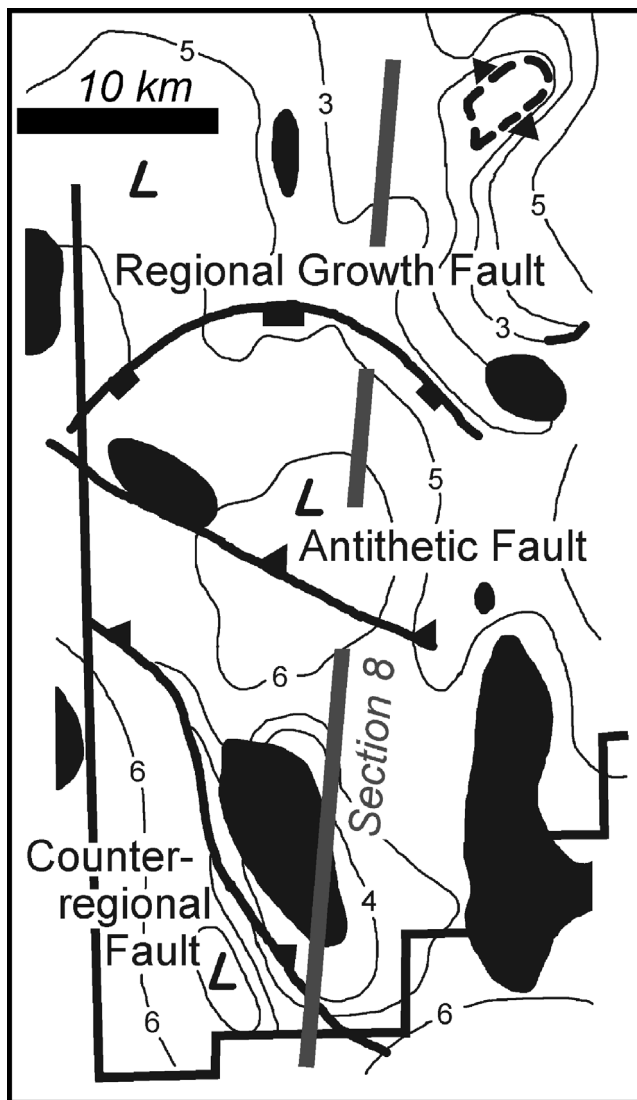


Figure 3. Geologic map of minibasin for the Gulf of Mexico minibasin model (after Rowan, 1995, his Figure 1). The map shows salt above 3 s and the salt weld in two-way traveltime. Minibasin lows are marked as L. The location for our section 8 is marked by a thick gray line and is the same as for Rowan's 2-D section from his 1995 paper (see Figure 8 in this chapter). Three faults incorporated into the Gulf of Mexico minibasin model are shown. The antithetic fault was not shown on Rowan's original map.

Figures 4 and 7) before sediment covered it. As sediment deposition occurred, this salt moved into salt domes on the periphery of the canopy, and parts of the canopy welded. The salt redistribution depicted in Figure 4 is estimated automatically and entirely from the present-day salt-weld distribution and sediment pattern.

The salt redistribution takes into account changes in sediment deposition across faults, as discussed

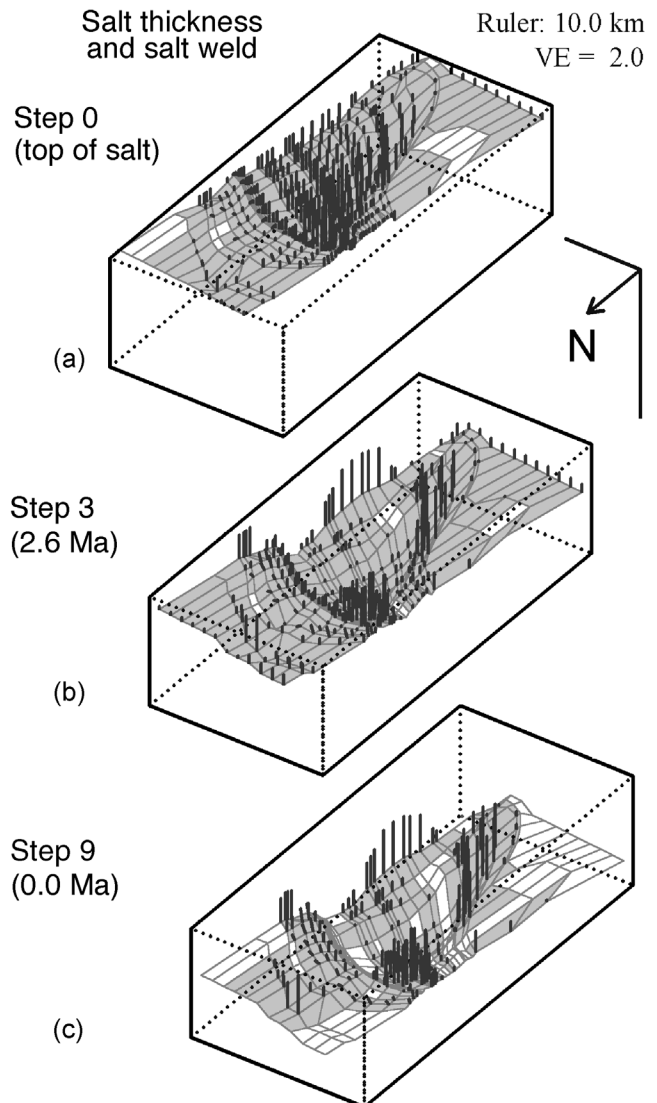


Figure 4. Isometric block diagrams of the 3-D restoration of the minibasin model using the automatic algorithm described in the text. View is from the northwest. Salt thickness is represented by bars grounded in the base-of-salt surface. The base of salt is shown as a surface with the finite-element grid superimposed. The surface is gray where salt is present and white where a salt weld formed. Figure 7 shows the evolution of section 8. Sections are numbered 1 through 12 from west to east; therefore, section 8 is the fifth section from the left. (a) Step 0: The model is completely backstripped to top of salt. Almost all the salt is concentrated as a thick salt canopy in the location where the minibasin will subsequently form. (b) Step 3: At 2.6 Ma, much of the salt has moved to the flanks of the minibasin and has been replaced by sediments. The basin is floored by a thin, nearly coherent salt sheet. See also Figure 7c. (c) Step 9: The model coincides with the input salt thickness. The basin floor is perforated by salt welds through which fluids can leak (see Figures 17 and 18).

above. The nature of faulting and our model description of it are shown in section and 3-D perspective in Figures 5 and 6, respectively. Figure 5 shows a detail of 2-D section 8 at three time steps. Two faults sole out into salt—the regional (south-dipping) growth fault in the north and its antithetic (north-dipping) fault in the south. The salt dome, at the base of the hanging wall in Figure 5a, shrinks with progressive faulting and provides accommodation space for fault throw. The section lengths within the first elements to the right of faults are not balanced.

The light gray layer (layer 9) in Figure 5 is deposited during step 3. The top of this layer is shown in isometric projection in Figure 6. In three dimensions, the regional growth fault is not only listric with depth but arcuate in shape, outlining the north-

ern boundary of the minibasin. During faulting, the layer surface is folded into a syncline on the hanging wall and into anticlines on the footwall (Figure 6b). The folding is caused by salt movement at depth. The fault gaps in the sediment layers progressively widen as the basin develops. The fault movements are automatically estimated by the preprocessor algorithms described above.

The salt movements estimated by our algorithms are compared with Rowan's in Figures 7 and 8. We comment on the two models at each stage of their development in the next few paragraphs.

Step 0, top of salt: Rowan (1995, his Figure 26a) starts with a schematic depiction of a bulb-shaped salt body above a hypothetical feeder stem. (His numeric reconstruction goes back to 3.8 Ma; see *Step 1*.)

BasinLAB's reconstruction of the initial salt mass complies with Rowan's idea that a bulbous allochthonous salt canopy evacuated with the sediment loading that produced the minibasin (Figure 7a). The bulb-shaped canopy is shown in 3-D in Figure 4a. Section 8 in Figure 7 is the fifth section from

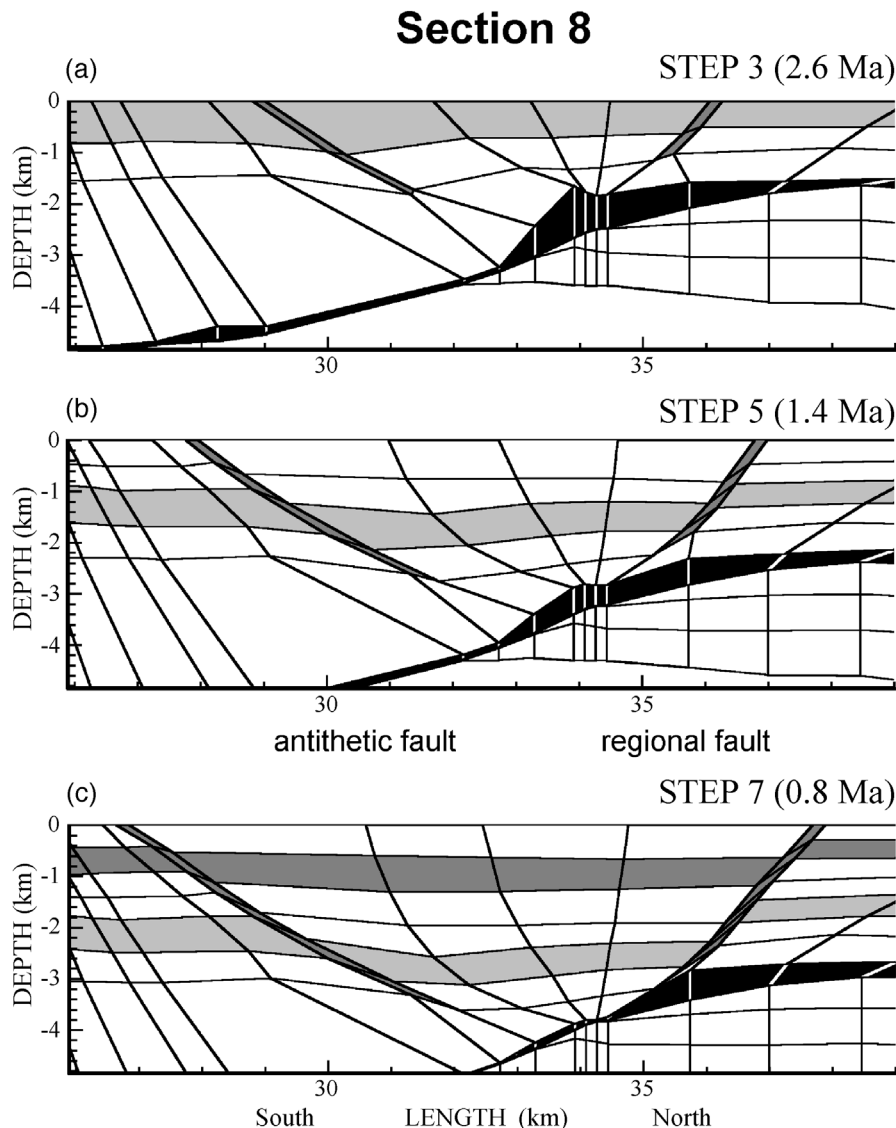


Figure 5. Two-dimensional faulting in the minibasin model. Fault macroelements are shown in dark gray and salt is shown in black. The section shows the regional, south-dipping fault to the right and its antithetic fault to the left. (a) Step 3: The layer deposited between 3 and 2.6 Ma (layer 9) lies at the surface and is colored light gray. (b) Step 5: At 1.4 Ma, layer 9 shows offset across both faults. (c) Step 7: At 0.8 Ma, the offset of layer 9 across the faults is greater. A second layer (darker gray layer 5), which was deposited at 1.1 Ma, also shows substantial offset across the faults. The figure illustrates important aspects of our faulting algorithm discussed in the text. Basin extension did not occur. Constant fault width is maintained, with the left side fixed and the right side moving into the elements to the right of the fault. Fault movement is facilitated by salt withdrawal.

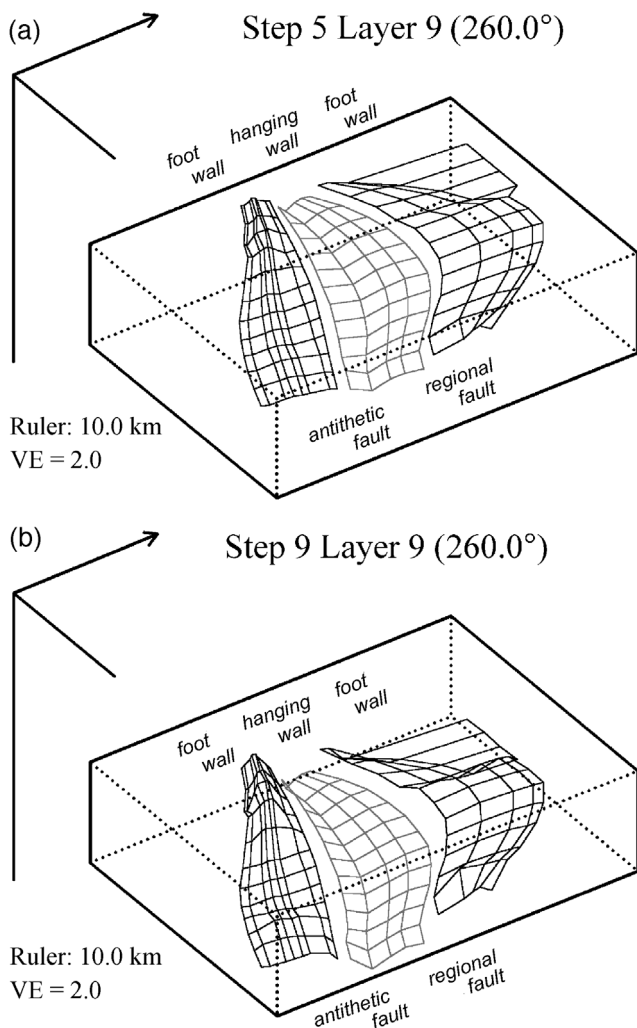


Figure 6. Isometric block diagrams of 3-D faulting in the minibasin model. The view is from the southeast. (a) Step 5: layer 9 (identified in Figure 5) is shown at 2.6 Ma. (b) Step 9: The present-day offset of layer 9. Faulting and salt movement have folded the surface into a syncline on the hanging wall and into anticlines on the footwall.

the east (left) or the eighth section from the west (right) in the 3-D model in Figures 4. Note that the section orientations in Figures 4 and 7 are potentially confusing but are indicated in the labels.

Step 1, 3.8 Ma: Rowan's reconstruction at this time step (Figure 8e) shows the incipient minibasin with a salt dome growing to the south. *BasinLAB's* reconstruction is identical (Figure 7b), except that the *BasinLAB* section is not contracted. Much of the minibasin and its southern salt dome developed in one time step in both reconstructions. This is because both reconstructions lack stratigraphic detail in the lower part of the section.

Step 3, 2.6 Ma: At this time, the minibasin is deeper, yet section 8 is still flooded by a coherent salt sheet (Figure 7c). Our reconstruction is nearly identical to that of Rowan (Figure 8d), including the appearance of a salt weld off the northern flank of the basin. The 3-D reconstruction (Figure 4b) shows that at this time, much of the salt has evacuated the minibasin, but that so far, there are only a few small salt welds on the floor of the basin.

Step 5, 1.4 Ma: Rowan's reconstruction (Figure 8c) shows a first salt weld in the northern minibasin along his 2-D line. In contrast, *BasinLAB's* reconstruction does not yet show a salt weld along this line (Figure 7d). In our reconstruction, both the regional fault and its antithetic fault are weakly active. The faults are centered at 130 km, with the regional fault dipping to the south. In Rowan's reconstruction, the antithetic fault is not yet active. Note that in his model, a considerable amount of basin extension has occurred without much offset across the faults. The extension is facilitated by shear within the salt layer. We neglect this extension, and this could be a reason for a somewhat later development of the salt weld in our analysis. The salt layer in our model may be thicker because of the lack of pure shear within the layer.

Step 7, 0.8 Ma: At this time, much of the minibasin is underlain by the salt weld, slightly more so in Rowan's reconstruction (Figure 8b) than ours (Figure 7e). Considerable movement has now occurred on all three major faults. The counterregional fault, above the southern salt dome, is active in both reconstructions. The throw of the faults is comparable in the two reconstructions.

Step 9, 0.0 Ma: Figure 7f shows our final modeling step. The minibasin is now flanked by salt masses on all sides. New salt welds perforate the basin floor, although most of the salt welds developed between Steps 5 and 7. Our basin description is as similar to Rowan's as we can make it in our gridding. Our model is constrained to recapture the initial geology of the section at the end of a simulation, so agreement with Rowan's section (Figure 8a) should be no surprise.

Although there are some minor differences, our automatic reconstruction of salt movement in Figure 7 is strikingly similar to Rowan's Figure 8. This does not mean that either reconstruction is right. Both could be wrong, and both undoubtedly failed to capture details not captured in the interpreted stratigraphy. In addition, our model, based

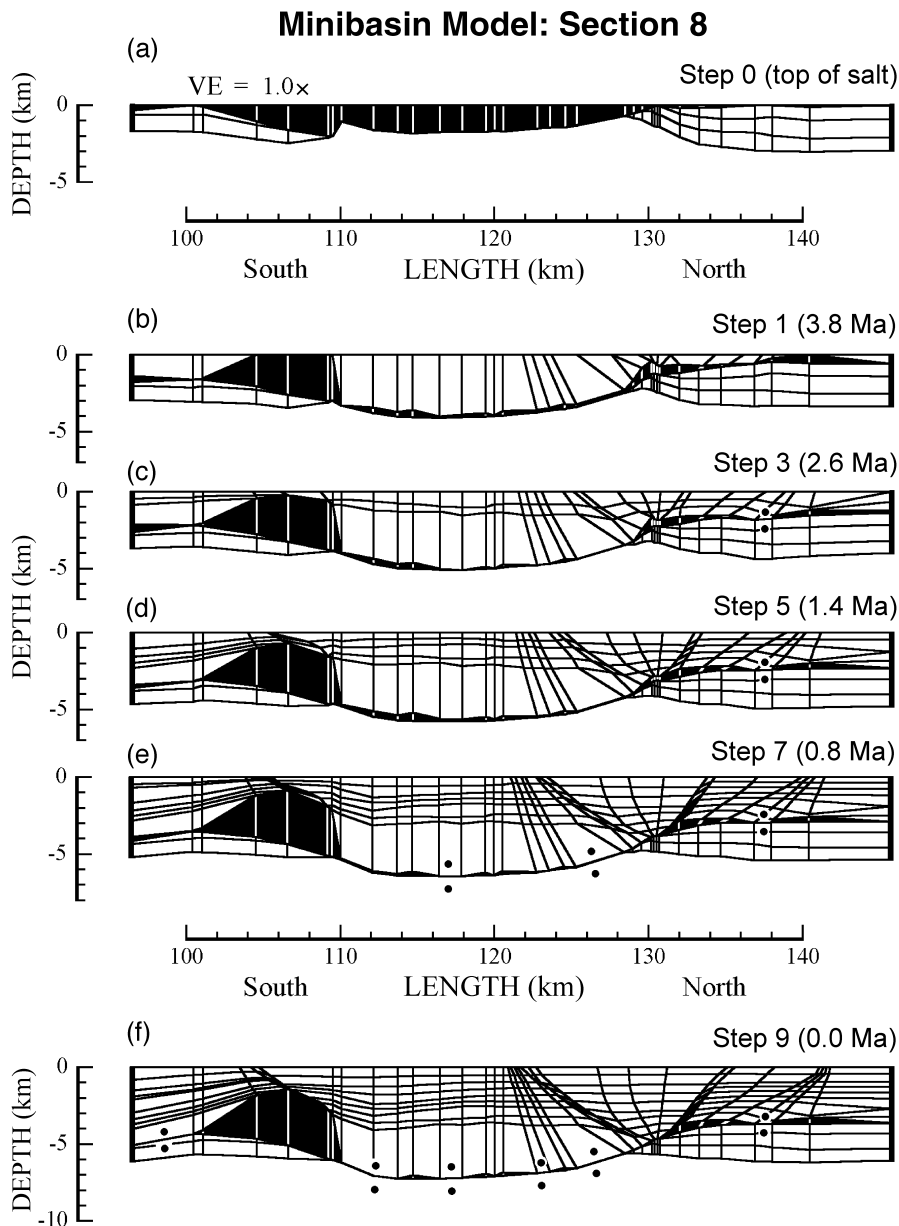


Figure 7. Three-dimensional restoration of the minibasin model, represented by section 8 of the 3-D model shown in Figure 4. (a) Step 0: The salt body prior to sediment deposition complies with Rowan's (1995) concept that the minibasin formed on a bulb-shaped, allochthonous salt canopy. (b) Step 1: The first step of the basin building shows the incipient minibasin with a salt dome growing to the left (south). (c) Step 3: A coherent salt sheet still underlies the minibasin. (d) Step 5: The minibasin is still floored by continuous salt. The salt dome in the south is being buried. Regional and antithetic faults are active (see also Figures 5b and 6a). (e) Step 7: Salt weld formation has begun within the minibasin. The antiregional fault in the south is active. For a detail of northern faults, compare with Figure 5c. (f) Step 9: The final step of the basin building is identical to the model input. Much of the minibasin lies on top of a salt weld. The automatic reconstruction shown in this figure is nearly identical to Rowan's reconstruction shown in Figure 8 of this chapter.

as it is on very simple rules for salt redistribution, could have obtained an appropriate result for the wrong reasons in this particular case. However, it is encouraging that our automatic model performed as well as it did, and because it is easy to use, it may be useful even if it eventually needs refinement in some of its details. We now illustrate its potential utility by analyzing salt movements in the larger (223×117 km) area shown in Figure 2.

APPLICATION TO REGIONAL SALT MOVEMENT

Geologic data used to define subsurface geology under the 223×117 -km area shown in Figure 2

were taken from two cross sections (lines X and Y in Figure 2) published by Mark G. Rowan (1996); four regional, interpreted seismic lines contributed to the GBRN by ARCO (lines A, B, C, and D in Figure 2); and a salt compilation by Gregory R. Simmons (1992). Rowan's (1996) line X was used for parts of our line 35 and his line Y was used for parts of our line 33. ARCO's lines A, B, C, and D formed the basis for our lines 41, 34, 27, and 22, respectively.

We used the minimum number of pseudowells required to define the salt geometry of the regional model. The pseudowell distribution is shown by dots in Figure 1. For example, a salt dome may be defined in three dimensions by a minimum of 18 pseudowells. Three pseudowells in each of three sections are required to define a "witch-hat" salt dome. The top and bottom surfaces of the salt must

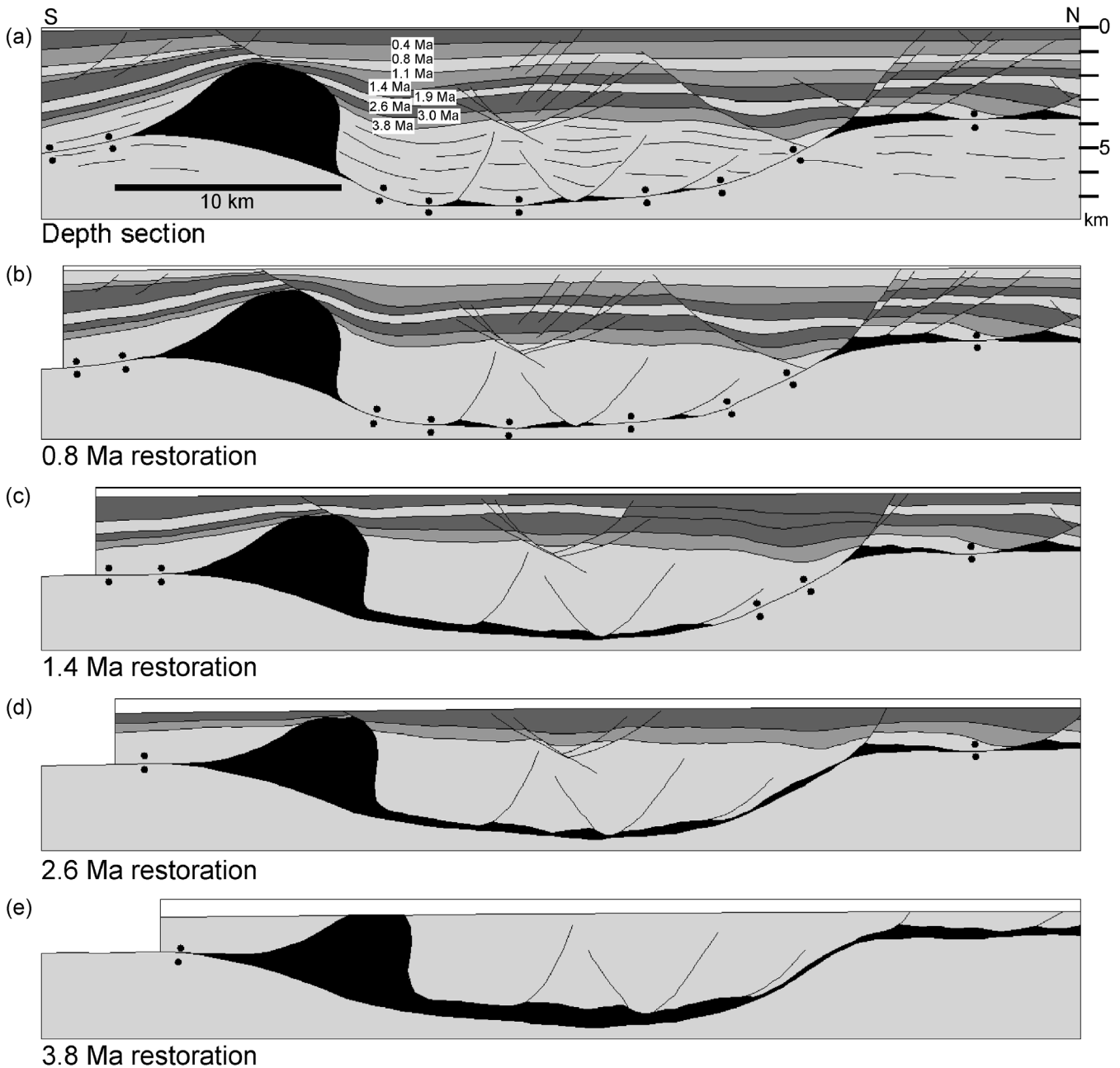


Figure 8. Reconstruction, with GEOSEC, by Rowan (1995) of the same 2-D line interpreted by our automatic salt reconstruction algorithm shown in Figure 7. (a) True scale 1:1 composite depth section constructed from parallel and adjacent north-south seismic profiles. This section served as input for our reconstruction. (b-e) Sequential restorations at same time steps as in Figure 7, but in reverse order, in accordance with the respective progressions of the modeling techniques used. The GEOSEC reconstruction includes a balanced section contraction back in time. This figure is reprinted from Rowan's Figure 24. AAPG © 1995. Reprinted by permission of the AAPG, whose permission is required for further use.

be defined. Hence, 18 nodes in nine pseudowells are required. The grid of the regional model is very coarse and interpolations are not always well constrained. In normal modeling practice, the "coarse" regional model would establish a framework and context for more refined, detailed smaller-scale models

embedded within it. Here, we simply illustrate construction of a 3-D model.

The geologic data in Simmons (1992), in the ARCO-interpreted seismic sections, and in Rowan's sections X and Y are in two-way seismic traveltime. We used a third-order polynomial to convert the

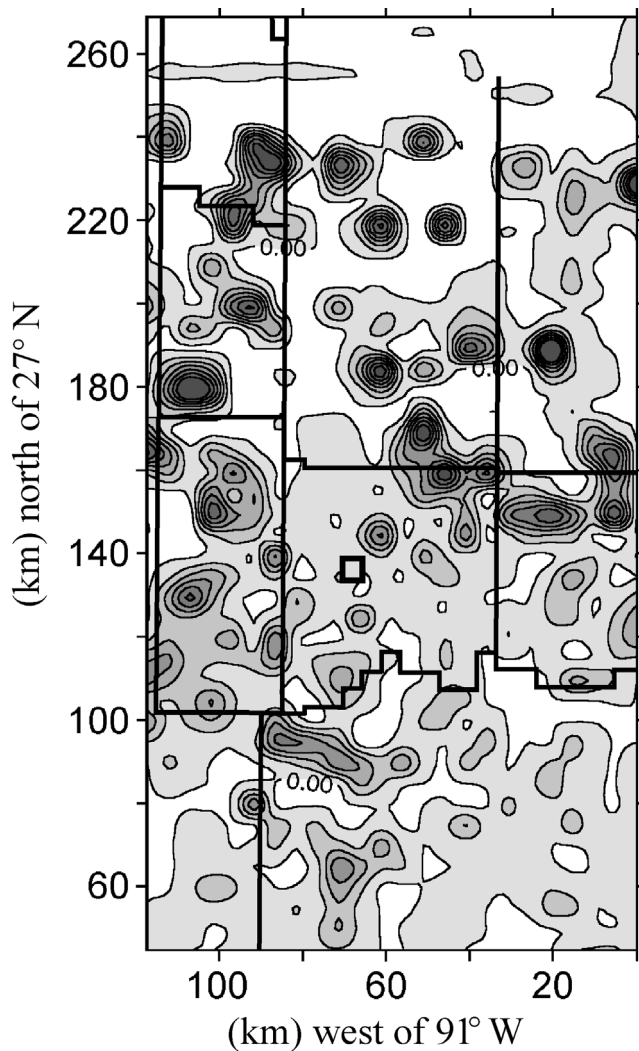


Figure 9. Isopach map showing salt thickness from the *BasinLAB* time-depth converted grid of the regional model. Contour interval is 1 km; white represents thickness of 0 km. Coordinate conventions are the same as in Figure 2, as are the overlay of lease block divisions and square for South Eugene Island Block 330 for spatial reference. Three distinct salt domains are visible: deep, isolated salt domes in the north; salt domes and salt welds within a shallower salt sheet in the middle; and an immature, shallow salt canopy in the south. These model salt thicknesses are largely based on Simmons (1992).

space-time grid to space-depth once the grid was input to *BasinLAB*. For this *BasinLAB* conversion, we derived an equation relating time and depth from 166 pairs of two-way traveltimes from 25 wells in and near the study area (Reed et al., 1987). This approach and the polynomial derived are similar to those described by Mann et al. (1987) and by Seni (1994).

Horizons were output and plotted from the geologic grid after it was converted from time to

depth. Isopachs derived from the horizons are shown in Figures 9, 11, and 12 and a depth map to the base of salt is shown in Figure 10. These maps give a visual impression of the sediment pattern driving salt movements in our model. The contouring program used kriging procedures.

The salt isopach map shown in Figure 9 illustrates very well that the northern third of the model has isolated, deep salt domes. The central part has a

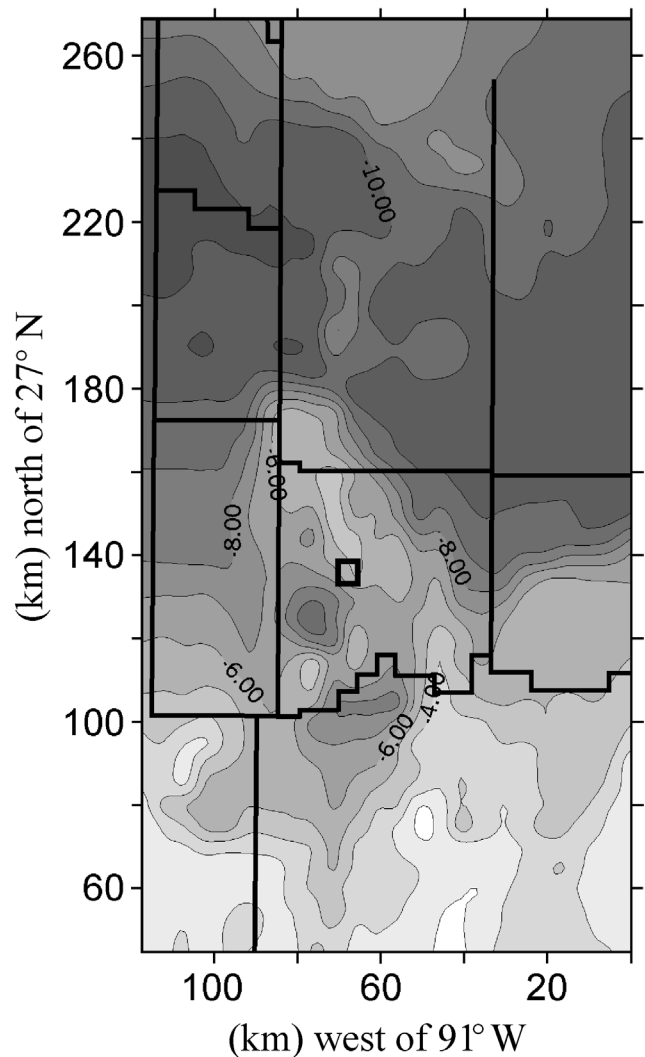


Figure 10. Map of the base salt from the *BasinLAB* time-depth converted grid of the regional model. Contour interval is 1 km; white represents depth of -2 km below water surface. Coordinate conventions are the same as in Figure 2, as are the overlay of lease block divisions and square for South Eugene Island Block 330 for spatial reference. The base of salt generally rises from north to south, except in the central part of the model, where the base may dip in almost any direction.

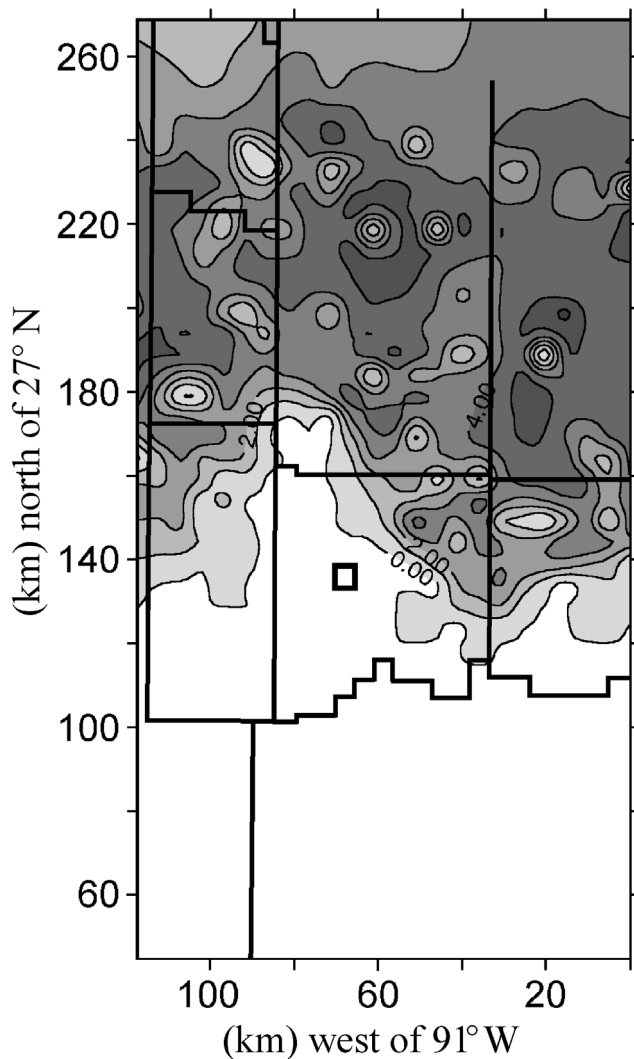


Figure 11. Isopach map of middle to upper Miocene sediments (13.4–5.6 Ma) with data from the *BasinLAB* time-depth converted grid of the regional model. Contour interval is 1 km; white represents thickness of 0 km. Coordinate conventions are the same as in Figure 2, as are the overlay of lease block divisions and square for South Eugene Island Block 330 for spatial reference. Sediment distribution is characterized by deep circular to crescent-shaped peripheral sinks around large, singular salt domes. Subsalt sediments of this age are not defined in this model (white area).

salt sheet, at a shallower level, which is perforated by salt welds and hosts salt domes. A very shallow, canopylike salt sheet covers the southern part of the model. Mature salt domes have not yet developed in this area.

Figure 10 shows that there is a general tendency for the salt horizon (including salt welds) in the regional model to rise from the north to the south.

A prominent exception is the structural high in the center of the modeled region. This high-lying base of the salt was hypothesized by Rowan (1995) to have been produced when salt rose along multiple and distinct salt feeders to form the canopy. The floors of present-day minibasins are the base of this original salt canopy. The salt base weld surface may dip in almost any direction in this area,

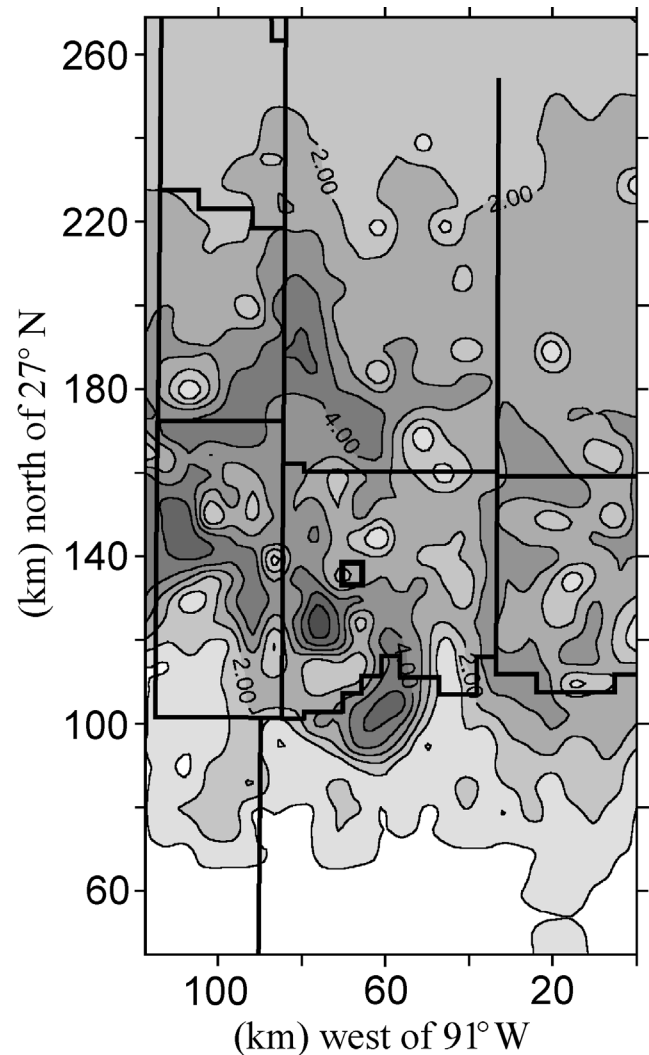


Figure 12. Isopach map of Pliocene sediments (5.6–1.7 Ma) from the *BasinLAB* time-depth converted grid of the regional model. Contour interval is 1 km; white represents thickness of 0 km. Coordinate conventions are the same as in Figure 2, as are the overlay of lease block divisions and square for South Eugene Island Block 330 for spatial reference. Large sediment basins are being formed at and just north of the present-day shelf break, e.g., just southwest of South Eugene Island Block 330. Subsalt sediments of this age are not defined in this model (white area).

and the regional model captures this undulating morphology.

Figure 9 shows the middle to upper Miocene (13.4–5.6 Ma) sediment distribution above the salt. Strata of this age are not present in the lower half of the figure because time-stratigraphic horizons are not defined below salt in our model. The southern edge of Miocene sediments thus appears to “pinch out” against the structurally rising salt sheet. This is not important. What is important is that the middle to upper Miocene isopachs show a very reasonable relation to salt diapirs. The deep salt domes in the north are surrounded by distinct, local depocenters. Sediments in these circular to crescent-shaped peripheral sinks have increased thickness. This sediment distribution is characteristic of salt domes, which have grown by downbuilding. Downbuilding is typical for active Gulf Coast salt diapirs (Seni, 1992), which grow as their associated minibasins fill.

Figure 12 shows that the line along which above-salt Pliocene (5.6 to 1.7 Ma) sediments abut salt has migrated south. The largest depocenter for this time

interval is adjacent to the South Eugene Island Block 330 (at 130 km north and 75 km west). Our analysis suggests that salt movements were active in this area in the Pliocene. Others have also suggested that salt-weld formation occurred in the late Pliocene in this area (Seni, 1992; Rowan, 1993).

The progressive development of salt welds on a regional scale, which is estimated by our salt redistribution algorithms, is shown in Figure 13. No welds are present at 8.3 Ma (Figure 13a). Welds form first in the north. By 1.7 Ma, the northern part of the model salt sheet is largely welded, but only a few welds have formed in the middle section and no welds have formed in the south (Figure 13b). This picture changes only slightly between 1.7 and 0.45 Ma (Figure 13c). Between 0.45 Ma and the present, a great many welds form in the middle and southern parts of our study area (Figure 13d). The distribution of welds at 0 Ma is taken as a given—a geologically known quantity that is input to the model. Thus, the distribution at 0 Ma has no great significance, but the formation of many welds between 0.45 and 0 Ma is a potentially important model estimation.

Salt movements in the regional model are further illustrated in two north-south sections in Figures 14 and 15. The *BasinLAB* reconstruction begins at step 0 when the basin is backstripped to the top of salt (Figures 14a and 15a). This stage is calculated without any significant age attached to it.

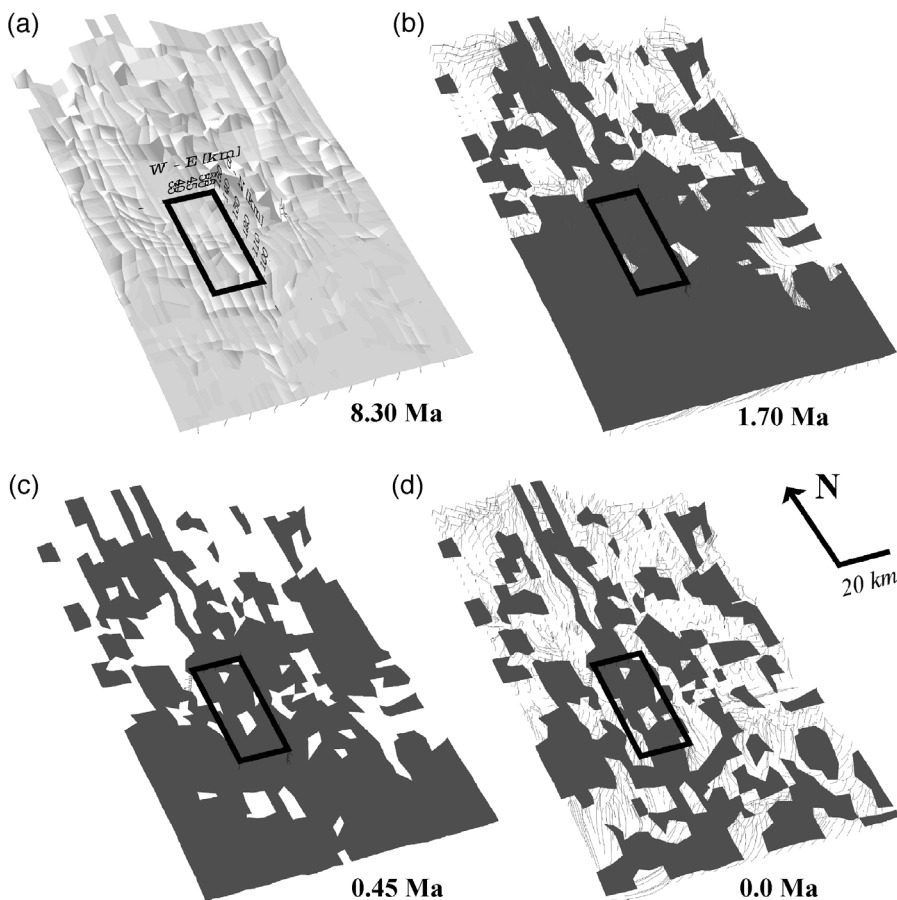


Figure 13. The progressive development of salt welds for the regional model. View from the southwest. Salt is shown in black; salt welds are shown in white, except in (a), which shows the top of salt as a surface illuminated from the north. No welds are present in the 8.30-Ma surface of (a). The formation of salt welds moves from the north at successively younger times. Most of the salt welds in the central and south-central areas formed between 0.45 Ma and the present. A black box outlines the minibasin model, which is analyzed at a higher resolution in Figures 4–8.

Salt does not intrude into sediments in our model; rather, the entire salt body forms one finite-element layer. Because no age is attached to this stage, the larger, autochthonous salt body in the north may not be genetically related to the smaller salt bodies in the central and southern parts of the section. The southern salt bodies may well have formed as allochthonous salt canopies, with salt supplied by separate feeder stems, as envisioned by Rowan (1995). Al-

though the salt is connected in the model along one continuous finite-element layer, these southern salt bodies may better be thought of as growing along imbricate salt ramps. These hypothetical ramps are neither modeled nor shown. Such subsalt structures could affect the calculated patterns of fluid flow, but our models do not include them. The simulations presented are simply limited in these regards at their present stage of development. Input of such features

can be done manually by the interpreter, but it is not automatic.

The development of a large, deeply rooted salt dome can be observed in the north of section 35 in Figure 14. The dome is

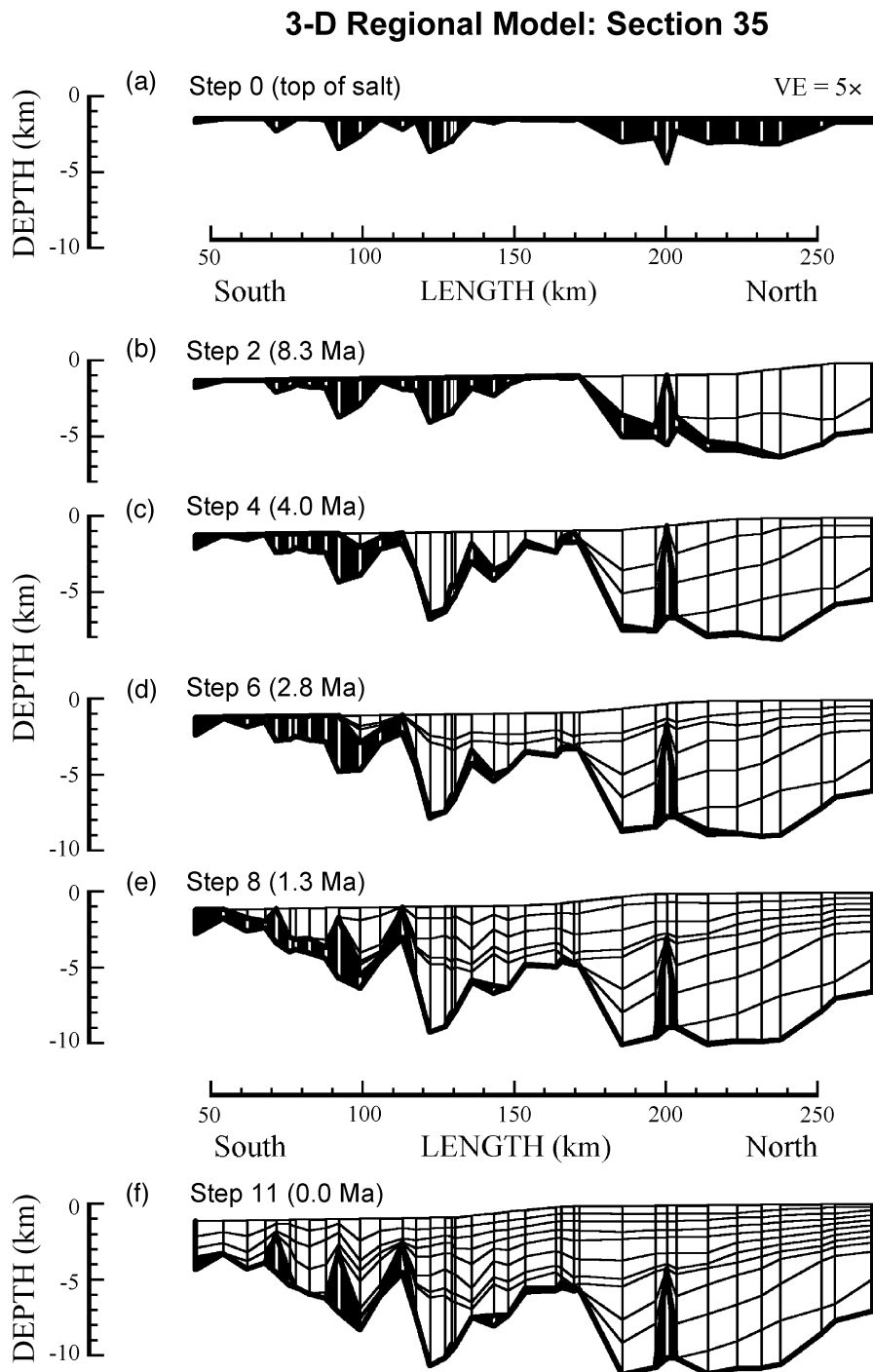


Figure 14. Three-dimensional restoration of the regional model, represented by section 35 of the 3-D model. Section 35 of the model includes Section Y interpreted by Rowan (1996). (a) Step 0: The model is completely backstripped to the top of salt. The salt in the north represents autochthonous salt; the salt in the south may be thought of as an allochthonous salt canopy. No age is attached to this configuration. (b) Step 2: A deeply rooted salt dome forms by downbuilding in the north. (c) Step 4: The dome in the north is still actively growing. Minibasins form in the central part in place of prior salt bodies and by burial of the forming salt-weld surface. The basal salt surface dips both south and north, as well as in and out of the section in three dimensions. (d) Step 6: At 2.8 Ma, the northern dome stops growing and is buried. In the central part of the section, salt is still slightly diminished by salt fall. (e) Step 8: By 1.3 Ma, salt movements near the South Eugene Island Block 330 area are nearly complete, and salt welds have formed. Basin formation began in the southern part. (f) Step 11: The section is identical to the model input. The salt structures and basins in the central part are mature and are being buried.

growing by downbuilding up to Step 5, i.e., it is growing at the same rate that the sediments aggrade around it, and thereafter the dome stops growing and is buried by younger sediments (Figures 5d, e). Salt domes stop growing with *BasinLAB*'s algorithm when no differential sediment load forces salt to move.

Minibasins start to form at 4.0 Ma in the central part of this section (between 105 and 170 km in

Figure 14c, and between 120 and 180 km in Figure 15c). From 4 to 1.3 Ma, salt domes in this area grow but undergo some salt fall because higher than average sedimentation rates force net salt evacuation (Figures 14e and 15e). From 1.3 Ma onward, the minibasins and their flanking salt masses undergo burial without further growth (Figures 14f and 15f).

The thick, young salt canopy in the south is disrupted by the formation of minibasins only when basin development is finished in the central part (Figures 14e and 15e). Salt tectonics is active here at the present day.

The development of section 33 (Figure 15) progresses in a manner similar to that of section 35. Section 33 contains South Eugene Island Block 330 at 135 km north or pseudowell 20 (wells are counted north to south). Although it is difficult to tell from the figure, a

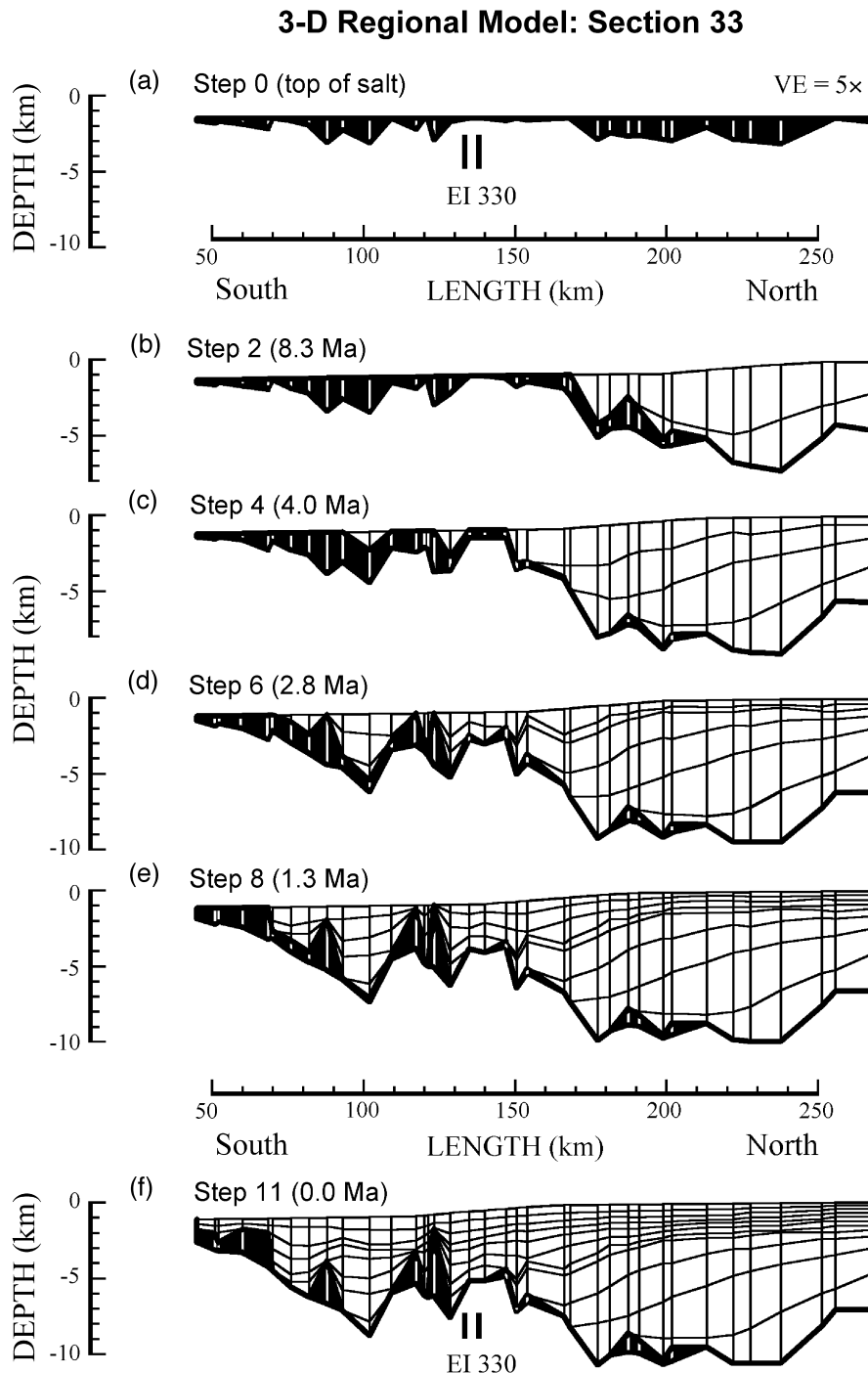


Figure 15. Three-dimensional restoration of the regional model, represented by section 33 of the 3-D model. Section 33 of the model includes section X interpreted by Rowan (1996). (a) Step 0: The model is back-stripped to the top of salt. The salt in the north represents autochthonous salt; the salt in the south may be thought of as allochthonous salt canopy. No age is attached to this configuration. (b) Step 2: Basin shows the rapid sedimentation to the north. (c) Step 4: A small minibasin forms in the central part of the section. (d) Step 6: At 2.8 Ma, salt domes are growing by downbuilding in the central part of the section and minibasins are developing. The basal salt sheet is still continuous. (e) Step 8: By 1.3 Ma, salt-weld formation has begun in the South Eugene Island Block 330 area. Basin formation begins in the southern part of the section. (f) Step 11: The section is identical to the model input. The salt structures and basins in the central part are mature and are being buried. Salt tectonics is still active in the southernmost part of the section.

salt weld opens between wells 19 and 20 at 1.3 Ma along the 2-D section 33 (Step 8, between 135 and 140 km in Figure 15e).

FLUID FLOW THROUGH THE EVOLVING SALT CANOPY

An important reason for investigating how the salt moved in the Gulf of Mexico is that the timing of salt-weld formation may control the migration or spillage of subsalt hydrocarbons into suprasalt traps. This is not the major intended part of this contribution, but we will briefly discuss some calculations that illustrate flow control by canopy evacuation and show how 3-D flow models can be integrated with 3-D salt migration models.

The models we show are simplified and heuristic. We consider pore-water flow, not hydrocarbon migration. The pore-water flow is driven by a combination of compaction and hydrocarbon maturation. The latter is more important. The hydrocarbon maturation is calculated assuming that a uniform total organic carbon content of all shales in the model is 0.4 wt.%. This is typical of shales in the South Eugene Island Area (Holland et al., 1990). Type II Burnham and Sweeney maturation kinetics is assumed and calculated for heat flows calibrated to vitrinite reflectance and bottom-hole temperature data in the Eugene Island Block 330 area (Coelho, 1997). The limited purpose of the maturation models is to produce a plausible fluid source distribution to drive pore fluid movements.

Flow is allowed through a salt weld in our 3-D models only if salt at all four corners of the weld has zero thickness. Figure 16 illustrates the importance of this convention. It is important because it means, for example, that a weld that appears to form in a 2-D section through one of our 3-D models might not be a weld in the sense that it allows 3-D model flow through the salt canopy.

The permeability of the strata below salt in the models presented is uniformly $1 \mu\text{d}$, a permeability six orders of magnitude higher than the permeability we assigned to salt. We believe this is a reasonably large-scale permeability for fractured shale. Because flow concentration to welds depends on the contrast between the permeability of salt and the subsalt strata, the focus of flow to welds will be similar to that shown in our calculations until the permeability of the subsalt strata enters the nanodarcy range and pore fluid pressures approach lithostatic. At this point, flow will be controlled by vertical hydrofractures,

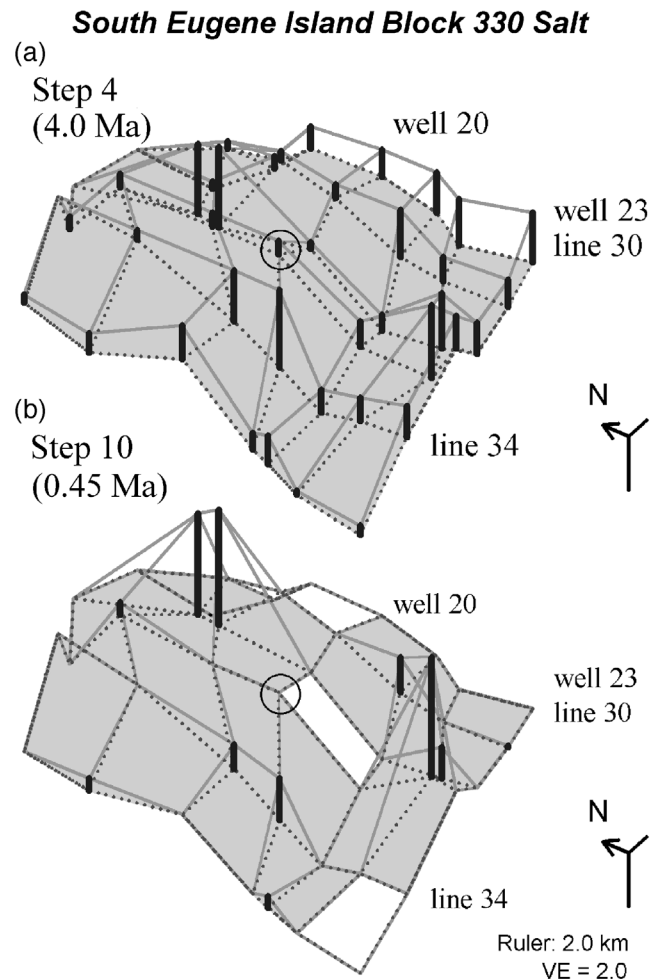


Figure 16. A partial view of the regional model illustrates the requirements for formation of a 3-D weld permeable enough to allow fluid throughput. The view is from the southwest. South Eugene Island Block 330 is located at the intersection of line 33 and well 20 (circled node). The top of salt is shown as solid lines, the base of salt as dotted lines. Salt thickness, where present, is indicated by thick vertical bars. Salt welds occur where dotted and solid lines merge. The base of the salt surface is shown as gray and is left white when welded. (a) At 4 Ma, the area is underlain by a continuous salt sheet with an uneven base and incipient salt domes. (b) At 0.45 Ma, the salt sheet has welded at South Eugene Island Block 330 and is surrounded by salt domes. Welds are considered formed when all nodes in a surface of a finite element are welded. A segment that is welded in a 2-D section only (edge of finite element) may not be a 3-D weld.

which could penetrate salt. We do not address this situation in this chapter.

Flow through the evolving salt sheet from subsalt strata with permeability of $1 \mu\text{d}$ was calculated for the entire regional (223×117 km) model, but we focus

our discussion on venting in the vicinity of the mini-basin submodel (box in Figures 2 and 13). Figure 17 shows flow vents through two distinct welds at 1.7 and 0.45 Ma. South Eugene Island Block 330 lies at 50 km east and 135 km north on the box scale in Figure 17, along the east side and in the upper third of the box and in approximately the same position as in the minibasin model grid in Figure 2. Figure 17a shows that there was major venting through a salt weld,

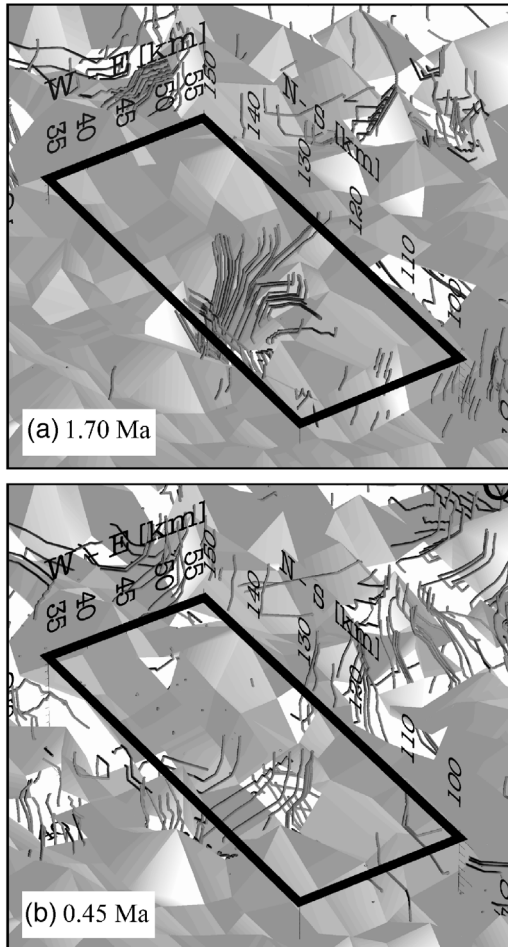


Figure 17. A close-up of the salt (gray), salt welds (white), and flow tubes (gray lines) for the mini-basin model area indicated in Figure 2. South Eugene Island Block 330 lies at 50 km east and 135 km north on the box scale. (a) A strong venting event is recorded at 1.70 Ma at both the western edge and the central part of the reference box. (b) At 0.45 Ma, the venting is weaker and goes through more salt welds. The weld at the eastern edge of the box at 130 km north vents fluids to the Eugene Island Block 330. The thick salt dome just to the north at 140 km coincides with the dome shown in the same position in Figure 16b. Note that the scale on the minibasin model box is different from the scale shown in Figure 2.

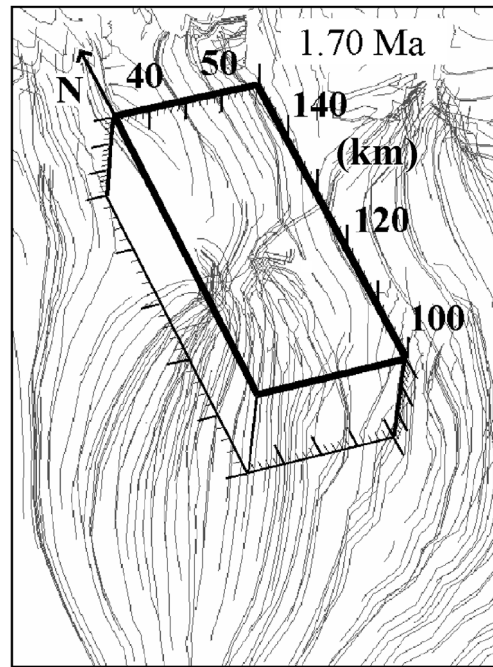


Figure 18. Close-up of tube flow within and around the same reference box as in Figure 17, but without the salt. The graph shows subsalt flow of brines toward the welds over distances in excess of 50 km. Subsalt permeability is a uniform $1 \mu\text{d}$ in our model simulations.

which opened at 1.7 Ma at the western edge of the box, as well as through a smaller salt weld in the central part of the box. There was less intense venting through these welds at 0.45 Ma (Figure 17b). The intensity of venting is indicated by the packing density of flow tubes.

Figure 18 shows how flow moves under the salt sheet to the salt welds at 1.7 Ma. The 25×50 -km box is again shown for geographic reference. This figure shows that the subsalt brines move horizontally over distances of more than 50 km to vent through particular salt welds. Although the model does not contain subsalt strata or structures, which could alter the flow directions significantly, the draw of fluids to salt welds is impressive.

DISCUSSION

Because our salt redistribution algorithm is based on the pattern of depression of the top-of-salt surface, the salt redistribution depends on sediment compaction parameters, the pattern of overpressuring (which affects compaction), and the flexural rigidity of the lithosphere, as well as the pattern of sediment deposition. We pick the best values for these parameters for the area modeled. We inferred

a flexural rigidity of 10^{23} Nm by modeling a 1200-km 2-D central Louisiana north-south section running from the Arkansas-Louisiana border to the Sigsbee Knolls. The compaction parameters were determined from well-log porosities by Coelho (1997). The parameter values could be slightly different from the values we selected, but changing their values will have much smaller impact on the salt redistribution estimated by our models than even minor changes in the suprasalt stratigraphy. The suprasalt sedimentation pattern is only weakly constrained by the data to which we have access, and is the major uncertainty in our modeling. In addition, it is not our purpose in this chapter to definitively model a particular area, but rather to illustrate a modeling method.

An important point related to parameter sensitivity is that the timing of salt-weld formation is not dependent on the present-day thickness of salt, but only on the suprasalt stratigraphy and the present distribution of salt welds. This lack of dependence on salt thickness is not intuitively obvious but is a logical consequence of the algorithm we describe. We have verified the independence on salt thickness by running the regional model with the present-day salt thickness increased and decreased by 30%. These changes produced negligible differences in the estimated time of salt-weld formation.

A second point that deserves comment is that 3-D models estimate significantly later salt-weld formation than 2-D models. The timing of weld formation calculated by our algorithms along a 2-D section in the Eugene Island area was 1.3 Ma. The timing of a complete weld surface in a 3-D finite-element mesh in the same location was calculated at 0.45 Ma. The difference results from trading of salt between 2-D lines and from the stricter criteria for welding over an entire element in 3-D (as opposed to welding only the side of an element in 2-D). The 0.45-Ma estimation of weld formation is in better agreement with geochemical evidence for filling of the Eugene Island Block 330 reservoirs within the last 0.23 Ma (S. Losh et al., personal communication, 1999). With our youngest time-stratigraphic horizon at 0.45 Ma and next youngest at 0.75 Ma, the resolution of late-weld formation is obviously very limited.

SUMMARY AND CONCLUSIONS

A simple algorithm for estimating 3-D salt movements is described, illustrated, tested, and applied in this chapter. The algorithm estimates the 3-D his-

tory of salt movement and the time of weld formation from the suprasalt stratigraphy to the present distribution of salt welds. Neither the predicted salt redistribution nor the weld timing depends on the current salt thickness. The critical operative assumption of the algorithm is that after isostatic adjustment is taken into account, accommodation space in areas having greater than average sediment loading is provided by salt movement to areas having less than average sediment loading.

The algorithm has many deficiencies. It presently adjusts salt in only one salt layer (although more could be added), and it does not account for or simulate many potentially important factors such as tectonic extension, salt buoyancy, salt overhangs, etc. Despite these deficiencies, we show that the salt movements it estimates compare almost exactly with reconstructions by others based on entirely different methods.

The algorithm is illustrated by application to a 223- × 117-km area of the offshore Louisiana Gulf of Mexico—an area far too large for salt movements to be modeled by nonautomated means. Gridding is kept as simple as possible, but nevertheless, important aspects of the sedimentation pattern are captured. The model shows a pattern of progressive salt migration and dome development that is directly linked to sediment progradation and aggradation. Regional differences in salt morphology are captured. Single, deep salt domes develop early in the north. Numerous salt welds and a base-of-salt/salt-weld surface, which dips in all directions, develop in the middle of our regional study area, as sedimentation progresses southward and loads the allochthonous salt sheet. The southernmost zone has a shallow salt canopy where the effects of sediment loading on diapirism are not yet played to the end.

Flow calculations show that salt welds could exert a major control on the flow of brines below the salt layer. The influence of welds is especially profound for the first welds to open. Subsalt brines can be drawn to these welds over distances of more than 50 km.

The most important attribute of the salt migration algorithm described and illustrated in this chapter is that it allows fully automatic, 3-D reconstruction of salt evolution and faulting. Automation may be particularly important because, as we show here, the estimated timing of weld formation can be much later in 3-D than in 2-D simulations. The 3-D salt reconstruction is labor intensive; therefore, automated methods are useful. With higher spatial and temporal

resolution definition of particularly the recent sedimentation pattern, the salt reconstruction methods described could predict the timing of weld formation accurately enough to be useful in oil and gas exploration.

ACKNOWLEDGMENTS

We are grateful to Jacqueline E. Huntoon for suggesting that differential sedimentation rates could be used to infer the rates of salt rise in the early stages of this project more than nine years ago. We thank ARCO Research for providing the interpreted sections used in this study to the Global Basins Research Network (GBRN). We thank Mark G. Rowan for providing original-scale copies of his sections for this study, as well as for discussions and for sharing his insights. The fluid-flow calculations were greatly facilitated by the initial work of François-Dominique Cipriani and the tireless advice and guidance of Paul D. Manhardt, CEO of GeoGroup, Inc., formerly of Computational Mechanics Corporation, and a finite-element expert. We thank Richard Buffler, who provided one of us (R.R.C.) with laboratory space and library access. The manuscript was very much improved by the thorough reviews and constructive comments of two AAPG reviewers, Chris Travis and an anonymous reviewer. We thank them for their efforts.

Although efforts to model regional salt redistribution started under the DOE Pathfinder project, support for the work reported here was provided almost entirely by the Gas Research Institute (GRI Grant No. 5097-260-3787) and the corporate sponsors of the GBRN. We are immeasurably indebted to these institutions for their support.

APPENDIX A

Following Palciauskas and Domenico (1989), porosity is modeled as a linear function of effective stress to a minimum porosity, ϕ_{\min} :

$$\phi = \phi_o - \sigma_{\text{eff}}/\sigma_c, \quad \text{for } \phi > \phi_{\min}. \quad (\text{A-1})$$

$$\phi = \phi_{\min}, \quad \text{for } \phi \leq \phi_{\min}. \quad (\text{A-2})$$

Here, ϕ_o is the uncompacted porosity of the mixed lithology, σ_{eff} is effective stress (lithostatic stress minus pore pressure), and σ_c is the inverse of compressibility. Sediments are characterized as mixtures of sand, shale, carbonate sand, and carbonate

mud. Salt is considered incompressible. For a mixed lithology,

$$\phi_o = \sum_{i=1}^4 f_i \phi_{oi}, \quad (\text{A-3})$$

$$\sigma_o = \sum_{i=1}^4 f_i \sigma_{ci}, \quad (\text{A-4})$$

where ϕ_i is the fraction of sand, shale, etc., and ϕ_{oi} and σ_{ci} are the uncompacted porosities and inverse compressibilities of the end-member lithologies (sand, shale, etc.). The parameters found suitable (Coelho, 1997) to describe compaction in the offshore Gulf of Mexico are shown in Table A-1.

Table A-1.

	<i>Uncompacted porosity</i> ϕ_o	<i>Inverse compressibility</i> σ_c (bars)
Sand	0.39	1750
Shale	0.35	1629

REFERENCES CITED

- Alexander, L. L., and P. B. Flemings, 1995, Geologic evolution of a Pliocene-Pleistocene salt-withdrawal minibasin: Eugene Island Block 330, offshore Louisiana: AAPG Bulletin, v. 79, p. 1737-1756.
- Cipriani, F. D., L. M. Cathles, and P. D. Manhart, 1993, Simulating salt diapirism, overpressuring, and seal rupture in sedimentary basins (abs.): EOS Transactions, American Geophysical Union, v. 74, p. 155.
- Coelho, D. F. S., 1997, Three dimensional analysis of the temperature field in Block 330, South Eugene Island, Gulf of Mexico: Ph.D. dissertation, Cornell University, Ithaca, New York, 292 p.
- Cornelius, R. R., L. M. Cathles, and F. D. Cipriani, 1993a, Salt tectonics, regional fluid flow, and oil migration offshore Louisiana, Gulf of Mexico (abs.): EOS Transactions, American Geophysical Union, v. 74, p. 155.
- Cornelius, R. R., J. E. Huntoon, F. D. Cipriani, and L. M. Cathles III, 1993b, Reconstruction of the evolution of part of the north-central Gulf of Mexico basin: The influence of salt movement on the stratigraphic record (abs.): EOS Transactions, American Geophysical Union, v. 74, p. 563.
- Cornelius, R. R., J. E. Huntoon, F. D. Cipriani, and L. M. Cathles, 1994, Effects of basin evolution on regional fluid flow and temperature history in the Gulf of Mexico, offshore Louisiana: AAPG 1994 Annual Convention, Denver, Colorado, June 12-15, p. 126.
- Galloway, W. E., D. G. Bebout, W. L. Fisher, J. B. Dunlap Jr.,

- R. Cabrera-Castro, J. E. Lugo-Rivera, and T. M. Scott, 1991, Cenozoic, *in* A. Salvador, ed., *The Gulf of Mexico Basin: Geological Society of America, Decade of North American geology*, v. J, p. 245–324.
- Holland, D. S., J. B. Leedy, and D. R. Lammlein, Eugene Island Block 330 Field—U.S.A. offshore Louisiana, 1990, *in* E. A. Beaumont and N. H. Foster, comps., *Structural traps III: Tectonic fold and fault traps: AAPG Treatise of petroleum geology, Atlas of oil and gas fields*, p. 103–143.
- Humphris, C. C. Jr., 1978, Salt movement on continental slope, northern Gulf of Mexico, *in* A. H. Bouma, G. T. Moore, and J. M. Coleman, eds., *Framework facies, and oil-trapping characteristics of the upper continental margin: AAPG Studies in Geology 7*, p. 69–85.
- Jackson, M. P. A., 1997, Conceptual breakthroughs in salt tectonics: A historical review, 1856–1993: University of Texas at Austin, Bureau of Economic Geology Report of Investigations No. 246, 51 p.
- Jackson, M. P. A., and R. R. Cornelius, 1987, Stepwise centrifuge modeling of the effects of differential sedimentary loading on the formation of salt structures, *in* I. Lerche and J. J. O'Brien, eds., *Dynamical geology of salt and related structures: Orlando, Florida, Academic Press*, p. 163–259.
- Jackson, M. P. A., and C. J. Talbot, 1991, A glossary of salt tectonics: University of Texas at Austin, Bureau of Economic Geology Geological Circular No. 91-4, 44 p.
- Jackson, M. P. A., R. R. Cornelius, C. H. Craig, and C. J. Talbot, 1987, The Great Kavir salt canopy: A major new class of salt structures: *Geological Society of America Abstracts with Programs*, v. 19, p. 714.
- Jackson, M. P. A., R. R. Cornelius, C. H. Craig, A. Gansser, J. Stoeklin, and C. J. Talbot, 1990, Salt diapirs of the Great Kavir, Central Iran: *Geological Society of America Memoir 177*, 139 p.
- Mann, R. G., W. R. Bryant, and P. D. Rabinowitz, 1987, Seismic stratigraphy and salt tectonics of the northern Green Canyon area, Gulf of Mexico: Texas A&M Department of Oceanography Technical Report 87-5-T, 218 p.
- McBride, B. C., P. Weimer, and M. G. Rowan, 1998, The effect of allochthonous salt on the petroleum systems of northern Green Canyon and Ewing Bank (offshore Louisiana), northern Gulf of Mexico: *AAPG Bulletin*, v. 82, p. 1083–1112.
- Nelson, T. H., 1991, Salt tectonics and listric-normal faulting, *in* A. Salvador, ed., *The Gulf of Mexico basin: Geological Society of America, Decade of North American geology*, v. J, p. 73–89.
- Palciauskas, V. V., and P. A. Domenico, 1989, Fluid pressures in deforming porous rocks: *Water Resources Research*, v. 25, p. 203–213.
- Reed, J. C., C. L. Leyendecker, A. S. Khan, C. J. Kinler, P. F. Harrison, and G. P. Pickens, 1987, Correlation of Cenozoic sediments Gulf of Mexico outer continental shelf, part I: Galveston area offshore Texas through Vermilion Area offshore Louisiana: New Orleans, U.S. Department of the Interior Minerals Management Service Gulf of Mexico OCS Regional Office, OCS Report MMS 87-0026, 35 p. plus 596 p. appendices.
- Roberts, S. J., J. A. Nunn, L. M. Cathles, and F. D. Cipriani, 1996, Expulsion of abnormally pressured fluids along faults: *Journal of Geophysical Research*, v. 101, p. 28231–28252.
- Rowan, M. G., 1993, A systematic technique for the sequential restoration of salt structures in extensional terranes: *Tectonophysics*, v. 228, p. 331–348.
- Rowan, M. G., 1995, Structural styles and evolution of allochthonous salt, central Louisiana outer shelf and upper slope, *in* M. P. A. Jackson, D. G. Roberts, and S. Snelson, eds., *Salt tectonics: A global perspective: AAPG Memoir 65*, p. 199–228.
- Rowan, M. G., 1996, Benefits and limitations of section restoration in areas of extensional salt tectonics: An example from offshore Louisiana, *in* P. G. Buchanan and D. A. Nieuwland, eds., *Modern developments in structural interpretation, validation and modelling: Geological Society of London Special Publication 99*, p. 147–161.
- Rowan, M. G., P. Weimer, and P. B. Flemings, 1994, Three-dimensional geometry and evolution of a composite, multi-level salt system, western Eugene Island, offshore Louisiana: *Transactions Gulf Coast Association Geological Societies*, v. 44, p. 641–648.
- Seni, S. J., 1992, Evolution of salt structures during burial of salt sheets on the slope, northern Gulf of Mexico: *Marine and Petroleum Geology*, v. 9, p. 452–468.
- Seni, S. J., 1994, Salt tectonics on the continental slope, northeast Green Canyon Area, northern Gulf of Mexico: Evolution of stocks and massifs from reactivation of salt sheets: University of Texas at Austin, Bureau of Economic Geology Report of Investigations No. 212, 102 p.
- Simmons, G. R., 1992, The regional distribution of salt in the northwestern Gulf of Mexico: Styles of emplacement and implications for early tectonic history: Ph.D. dissertation, Department of Oceanography, Texas A&M University, College Station, Texas, 180 p.
- Talbot, C. J., 1992, Centrifuge models of Gulf of Mexico profiles: *Marine and Petroleum Geology*, v. 9, p. 412–432.
- Talbot, C. J., 1993, Spreading of salt structures in the Gulf of Mexico: *Tectonophysics*, v. 228, p. 151–166.
- Turcotte, D. L., and G. Schubert, 1982, *Geodynamics*: New York, John Wiley & Sons, 450 p.
- Vendeville, B. C., and M. P. A. Jackson, 1992a, The rise of diapirs during thin-skinned extension: *Marine and Petroleum Geology*, v. 9, p. 331–353.
- Vendeville, B. C., and M. P. A. Jackson, 1992b, The fall of diapirs during thin-skinned extension: *Marine and Petroleum Geology*, v. 9, p. 354–371.